AGU ADVANCING EARTH AND SPACE SCIENCE

Geophysical Research Letters®

RESEARCH LETTER
10.1029/2022GL098821

Special Section:
ExoMars Trace Gas Orbiter - One Martian Year of Science

Planet-Wide Ozone Destruction in the Middle Atmosphere on Mars During Global Dust Storm

F. Daerden[1], L. Neary[1], M. J. Wolff[2], R. T. Clancy[2], F. Lefèvre[3], J. A. Whiteway[4], S. Viscardy[1], A. Piccialli[1], Y. Willame[1], C. Depiesse[1], S. Aoki[5], I. R. Thomas[1], B. Ristic[1], J. Erwin[1], J.-C. Gérard[6], B. J. Sandor[2], A. Khayat[7], M. D. Smith[7], J. P. Mason[8], M. R. Patel[8], G. L. Villanueva[7], G. Liuzzi[7,9], G. Bellucci[10], J.-J. Lopez-Moreno[11], and A. C. Vandaele[1]

[1]Royal Belgian Institute for Space Aeronomy BIRA-IASB, Brussels, Belgium, [2]Space Science Institute, Boulder, CO, USA, [3]LATMOS, Sorbonne Université, UVSQ Université Paris-Saclay, CNRS, Paris, France, [4]Centre for Research in Earth and Space Science, York University, Toronto, ON, Canada, [5]Institute of Space and Astronautical Science ISAS, Japan Aerospace Exploration Agency JAXA, Sagamihara, Japan, [6]LPAP, STAR Institute, Université de Liège, Liège, Belgium, [7]NASA Goddard Space Flight Center, Greenbelt, MD, USA, [8]School of Physical Sciences, The Open University, Milton Keynes, UK, [9]Department of Physics, School of Arts and Sciences, American University, Washington, DC, USA, [10]Istituto di Astrofisica e Planetologia Spaziali, IAPS-INAF, Rome, Italy, [11]Instituto de Astrofisica de Andalucia, IAA-CSIC, Granada, Spain

Key Points:

- NOMAD ozone (O_3) data filtering during the 2018 global dust storm shows strong O_3 destruction compared to one year later with no dust storm
- 3D simulations of atmospheric chemistry in the 2018 global dust storm are presented to understand impact on odd hydrogen and odd oxygen
- The model confirms middle-atmospheric O_3 destruction in the dust storm and predicts increased photochemical production of hydrogen

Supporting Information:

Supporting Information may be found in the online version of this article.

Correspondence to:

F. Daerden,
Frank.Daerden@aeronomie.be

Citation:

Daerden, F., Neary, L., Wolff, M. J., Clancy, R. T., Lefèvre, F., Whiteway, J. A., et al. (2022). Planet-wide ozone destruction in the middle atmosphere on Mars during global dust storm. *Geophysical Research Letters*, *49*, e2022GL098821. https://doi.org/10.1029/2022GL098821

Received 22 MAR 2022
Accepted 20 MAY 2022

Author Contributions:

Conceptualization: F. Daerden
Data curation: F. Daerden, L. Neary, M. J. Wolff, I. R. Thomas, B. Ristic
Formal analysis: F. Daerden, M. J. Wolff
Investigation: F. Daerden, M. J. Wolff, R. T. Clancy, F. Lefèvre, J. A. Whiteway
Methodology: F. Daerden, M. J. Wolff

Abstract

The Nadir and Occultation for MArs Discovery (NOMAD)/UV-visible (UVIS) spectrometer on the ExoMars Trace Gas Orbiter provided observations of ozone (O_3) and water vapor in the global dust storm of 2018. Here we show in detail, using advanced data filtering and chemical modeling, how Martian O_3 in the middle atmosphere was destroyed during the dust storm. In data taken exactly 1 year later when no dust storm occurred, the normal situation had been reestablished. The model simulates how water vapor is transported to high altitudes and latitudes in the storm, where it photolyzes to form odd hydrogen species that catalyze O_3. O_3 destruction is simulated at all latitudes and up to 100 km, except near the surface where it increases. The simulations also predict a strong increase in the photochemical production of atomic hydrogen in the middle atmosphere, consistent with the enhanced hydrogen escape observed in the upper atmosphere during global dust storms.

Plain Language Summary

Global dust storms are rare but impactful events on Mars, occurring about once in a decade. Previous investigations found how water vapor is redistributed throughout the entire atmosphere in a dust storm. Photolysis of water vapor by sunlight produces highly reactive species that destroy ozone (O_3). Here we present O_3 measurements taken by the NOMAD/UVIS instrument on the ExoMars Trace Gas Orbiter in the 2018 global dust storm. After advanced data filtering, they demonstrate how O_3 in the middle atmosphere was much reduced compared to one Mars year later when no dust storm occurred. 3D atmospheric model simulations of atmospheric chemistry in the global dust storm confirm this planet-wide O_3 destruction, and help to understand the involved processes. The simulations also predict a strong increase in production of atomic hydrogen in the middle atmosphere, that can explain the observed increased hydrogen atmospheric escape during global dust storms.

1. Introduction

Water vapor (H_2O) is only a trace species on Mars, with abundances of at most a few parts per thousand in an otherwise carbon dioxide (CO_2) dominated atmosphere. However, it plays a key role in Mars' atmospheric chemistry. Indeed, CO_2 is subject to photolysis and its current abundances cannot be explained without assuming that its photolysis product carbon monoxide (CO) is recycled into CO_2 through a reaction with OH, a radical resulting from photolysis of water vapor (McElroy & Donahue, 1972; Parkinson & Hunten, 1972). Another relatively abundant trace gas on Mars is ozone (O_3), but it is over a thousand times less abundant than water vapor on Mars, and over a hundred times less abundant than O_3 on Earth. Ozone is mainly produced by the three-body reaction of atomic (O) and molecular (O_2) oxygen in the presence of CO_2. Yet fast reactions involving odd hydrogen species (H, OH and HO_2, or HO_x) resulting from water photochemistry will readily destroy O_3 or suppress its formation in catalytic cycles, making water vapor the key species in controlling the abundance of O_3. In the lower atmosphere, there is sufficient CO_2 (i.e., pressure) to maintain large O_3 concentrations, but its abundance

Resources: F. Daerden, L. Neary, M. J. Wolff, I. R. Thomas, B. Ristic
Software: F. Daerden, L. Neary, M. J. Wolff
Supervision: F. Daerden
Validation: F. Daerden, M. J. Wolff
Visualization: F. Daerden, L. Neary, R. T. Clancy, F. Lefèvre
Writing – original draft: F. Daerden
Writing – review & editing: F. Daerden, L. Neary, M. J. Wolff, R. T. Clancy, F. Lefèvre, J. A. Whiteway, J. Erwin, J.-C. Gérard, B. J. Sandor, M. R. Patel

decreases with height. This effect is strengthened by an increase in the photolysis rate coefficient of water vapor with height. At the same time, water vapor frequently deposits into ice clouds below ∼40 km (height changing with latitude and season) and becomes only sparsely available above the cloud zone. In that region, the O_3 formation is no longer suppressed, and its abundances will increase with height, although limited by the decreasing CO_2 density (Daerden et al., 2019; Khayat et al., 2021; Lefèvre et al., 2004; Patel et al., 2021; Clancy and Nair, 1996).

Until recently, O_3 was observed mostly for its total column abundances (Lefèvre et al., 2021; Montmessin et al., 2017; Perrier et al., 2006; Clancy et al., 2016; Willame et al., 2017) and in some cases for its vertical profile (Lebonnois et al., 2006; Montmessin & Lefèvre, 2013). The start of science operations of the ExoMars Trace Gas Orbiter (TGO) in 2018 formed a landmark change in the knowledge of O_3 on Mars. TGO carries two sensitive spectrometer suites, Nadir and Occultation for MArs Discovery (NOMAD, Vandaele et al., 2018, 2019) and Atmospheric Chemistry Suite (ACS, Korablev et al., 2018, 2019). The UV-visible (UVIS) channel of NOMAD monitors the vertical profile of O_3 on a daily basis with the solar occultation technique (Khayat et al., 2021; Patel et al., 2021). Water vapor profiles are measured simulateanously with the NOMAD IR channel (Aoki et al., 2019). In addition, the IR channel of ACS could retrieve O_3 in some cases (Olsen et al., 2020).

Dramatic changes in the vertical distribution of water vapor during global dust storms (GDS) were first reported by the SPICAM instrument on Mars Express (Fedorova et al., 2018) for the 2007 GDS, and more recently by the TGO (Aoki et al., 2019; Fedorova et al., 2020; Vandaele et al., 2019) and SPICAM (Fedorova et al., 2021) for the 2018 GDS. As the planet's atmosphere contains much more dust, solar radiative heating by the dust changes the temperatures considerably (Smith, 2019) compared to the same season without a GDS. This has a dramatic impact on water vapor, as the increased temperatures prevent cloud formation, and water vapor is transported to much larger heights and, following the global circulation (which is also enhanced in dust storms), to higher latitudes, up to the polar regions. This phenomenon was simulated in a General Circulation Model (GCM), producing a good agreement with the water observations of NOMAD during the 2018 GDS (Neary et al., 2020).

The strong photochemical relationship between water vapor and O_3 implies that the redistribution of water vapor during the GDS will also have an impact on O_3. A first analysis of NOMAD/UVIS O_3 profiles taken during the GDS (Patel et al., 2021) found that mid- and high-latitude O_3 abundances above 20 km were reduced in the GDS compared to 1 year later, when no GDS occurred. Here we perform new retrievals of the O_3 profiles that allow us to increase the signal-to-noise through spectral and spatial binning, and to develop an improved data filtering. Both of these facets are particularly helpful for the lower transmittances found in dusty conditions, and so to provide a clearer picture in the 2018 GDS. We will also investigate the behavior of odd hydrogen and odd oxygen (including O_3) using a GCM that is operated for the conditions of Martian years (MY) 34 and 35 (Daerden et al., 2022; Neary et al., 2020) and that includes detailed atmospheric chemistry routines (Daerden et al., 2019). Combining the filtered observations with the model simulations then allows to obtain a detailed picture of the changes in atmospheric chemistry during the 2018 GDS.

2. Ozone Retrieval and Data Filtering

The NOMAD/UVIS spectrometer operates in the UVIS domain between wavelengths 200–650 nm. It has two observation modes with different sensitivity: the solar occultation mode and nadir/limb viewing mode. In this study only observations made with the solar occultation channel are considered. Details and characteristics of the NOMAD/UVIS instrument, its solar occultation channel, and calibration were presented in various publications (Gérard et al., 2020; Khayat et al., 2021; Patel et al., 2017, 2021; Vandaele et al., 2018).

We perform the retrievals of O_3 profiles in a manner that is equivalent to previous work (Khayat et al., 2021; Patel et al., 2021), but different in detail. First, we derive extinction profiles by applying the so-called "onion-peeling" method to the NOMAD/UVIS transmittance spectra, as was described for TGO/ACS observations (Stcherbinine et al., 2020). In essence, an upper triangular matrix is formed (at each wavelength) using a spherically symmetric atmospheric shell model, which is solved analytically to produce vertical profiles of opacity with error propagation given by equation 7 of Stcherbinine et al. (2020). The column density of O_3 in each layer is then determined by fitting a model of a linear continuum plus O_3 absorption (Sander et al., 2011) to the data between 240 and 320 nm. The best-fit solution is found using a Marquardt-Levenberg algorithm, as implemented in the package MPFIT (Markwardt, 2009). The uncertainty associated with the derived O_3 densities (and linear fit parameters) is provided by MPFIT from the diagonal terms of the covariance matrix. Extensive comparisons of our

retrievals outside of dusty conditions with the published full NOMAD/UVIS O_3 data set (Khayat et al., 2021; Patel et al., 2021) showed good agreement within the uncertainties of each retrieval. The data set presented in this paper, with full retrieval and filtering (see below) details, is publicly available (Daerden & Wolff, 2022).

The motivation to develop our own retrieval process was the ability to perform sensitivity analyses and develop additional filters to remove spurious O_3 detection. Such spurious detections (i.e., O_3 detection without an O_3 signature present in the transmission spectra) were found to occur in regimes where the opacity spectra can be quite noisy. In other words, relying on the covariance matrix alone for our retrievals was not sufficient, since it can produce unphysical results. In this direction, we have taken two approaches. In addition to the formal uncertainty returned by MPFIT, we calculate an empirical equivalent to the information content approach (Rodgers, 2000) by comparing the χ^2 of the O_3 retrieval for each altitude to that of a linear-only model such that values less than one indicate that allowing O_3 provides a better fit, that is, $m = \chi^2(O_3 + \text{linear})/\chi^2(\text{linear}) < 1$. In other words, if a linear model fits as well (or better) than the O_3 model, the retrieved value is not statistically significant. We also allow for the binning of transmittance data in both wavelength and height, where the latter dimension is particularly effective in reducing the noise in the O_3 retrievals when the observations employ a large number of positions per occultation. We generally employed bins of 10 nm and 4 km. A somewhat similar analysis to ours presenting an information content approach to the full NOMAD/UVIS O_3 data set is in preparation by A. Piccialli et al.

Through numerical experimentation, we developed the following data filtering criteria. Data are removed from a profile if (a) the average transmittance between 240 and 320 nm was below 0.02, and (b) when $m = \chi^2(O_3 + \text{linear})/\chi^2(\text{linear}) > 0.7$, except during the period of April–November 2018 (which suffered from reduced signal-to-noise ratio) where we use $m > 0.85$. Outside of this period, the value of 0.7 is preferred since it provides a more consistent removal of spurious data points. Both m values are the result of substantial trial-and-error processes which include manual inspection of many (e.g., hundreds) individual profile fits per experiment. (c) A final step in the filtering process is done when the retrieved O_3 number density was less than the uncertainty returned by MPFIT.

3. Ozone in the Global Dust Storm

The observations are shown in Figure 1 for latitude bands >45°N and <45°S respectively, for the period before and during the 2018 GDS (in Mars year, MY, 34) and in the same season exactly one Martian year later (MY35), when no GDS occurred. The latitude of the observations changes over time, and their geospatial distribution in both years is shown in Figure S1 in Supporting Information S1. The choice to show the latitude bands poleward of 45° resulted from a compromise to minimize the mixing of data taken at different latitudes while maintaining a sufficiently dense temporal coverage of the profiles. Figure 2 shows the observations for all latitudes, but averaged over wider L_s intervals. The data are plotted using the height above the MOLA Mars reference level (Smith et al., 1999) as vertical coordinate, in order to combine observations taken over a variety of latitudes and longitudes (and hence for different surface heights). The observation errors for the data shown in both figures are shown in Figures S2 and S3 in Supporting Information S1.

In the period before the 2018 GDS (L_s = 160°–187°, Figure 1 and Figure 2a,b), a distinct O_3 minimum between 30 and 50 km (height varying with time and latitude) can be seen in each hemisphere at high latitudes in both years, with O_3 remaining abundant above this minimum up to 50–60 km (height again varying with time and latitude, this is the high altitude O_3 layer that was discussed before, Khayat et al., 2021). This pattern is present in both Mars years, but in MY34, at southern latitudes, it is less apparent because of the sparse observations in this case (Figure S1 in Supporting Information S1). The minimum in O_3 is associated with an observed and simulated maximum in water vapor in this region that is caused by transport of wet air along the ascending branches of the Hadley circulation cells (Aoki et al., 2019; Daerden et al., 2019; Neary et al., 2020). At these heights, water is more easily photolyzed and produces odd hydrogen species that both destroy and suppress O_3 formation (Daerden et al., 2019).

Observational constraints imposed by the orbital geometry of the TGO spacecraft caused gaps in the data of up to ~15° wide in L_s (at different times of the year in MY34 and MY35, see Figure 1), complicating the comparison of the 2 years over certain L_s ranges. Nevertheless, it is seen that in MY35 the ozone peak abundances above 30 km continue through to L_s = 230° after which the observable ozone above 30 km gradually disappears (Figures 1b and 1d). Figure 2d confirms this seasonal behavior in MY35, with a similar ozone distribution as before L_s = 187°

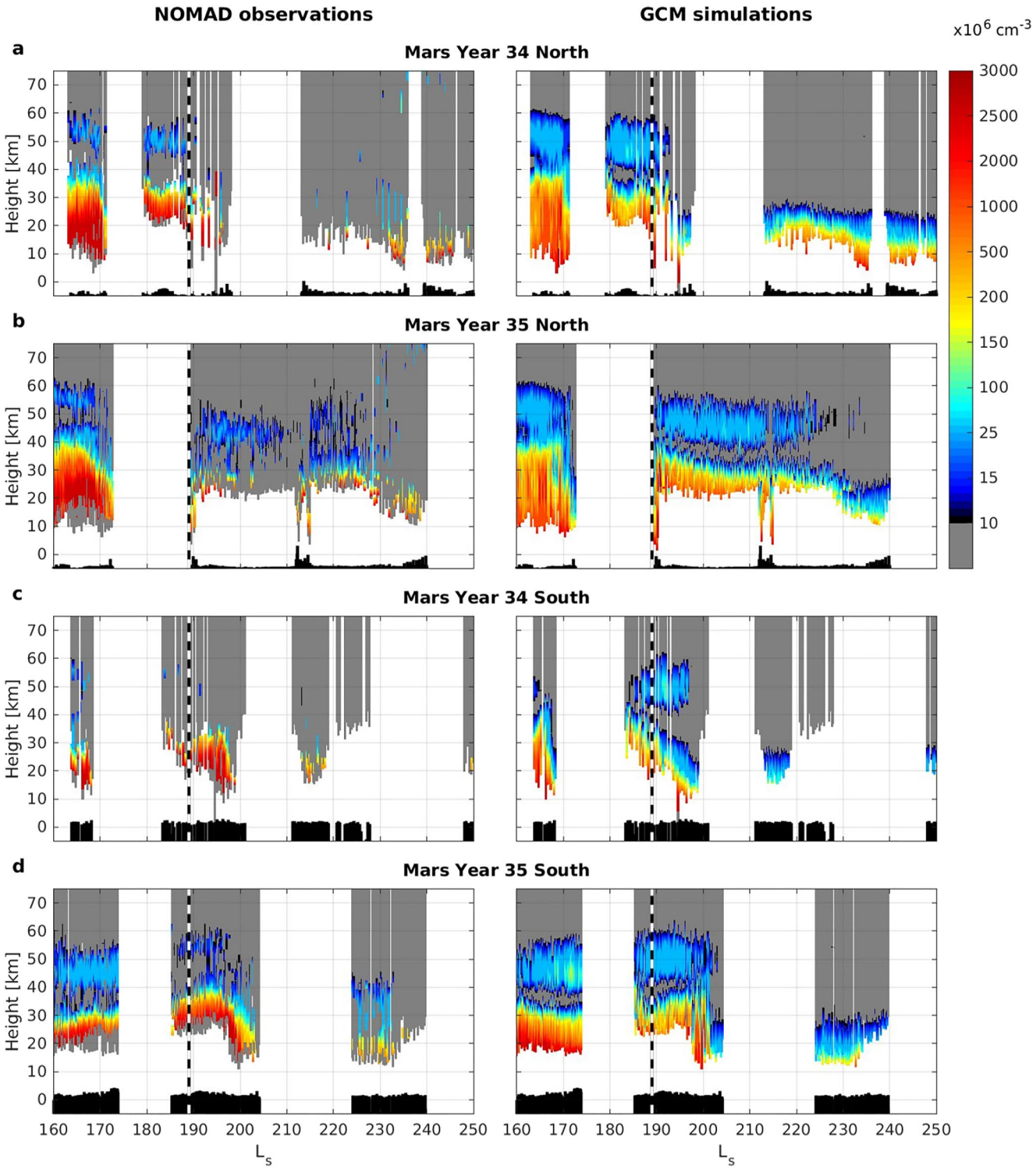

Figure 1. Time series of the ozone (O_3) number density profiles. Panels (a and b) for latitudes north of 45°N, for the same season in Mars year 34 (a, with GDS) and in Mars year 35 (b). Panels (c and d) show the same for latitudes south of 45°S. Left plots for the O_3 observed by NOMAD/UVIS and right ones from simulations. Gaps in the data are due to observational restrictions imposed by orbital geometry of the Trace Gas Orbiter spacecraft. Gray shading: for the observations, this represents values that were filtered out (see Section 2) or are below 10^7 cm^{-3}; for the simulations, values are below 10^7 cm^{-3}. Height is taken with respect to the MOLA reference level (black shading at the bottom of the panels shows the actual surface). Model results were interpolated to the time and location of the observations. The thick vertical dashed lines indicate the onset of the global dust storm in MY34 and the same time one Mars year later.

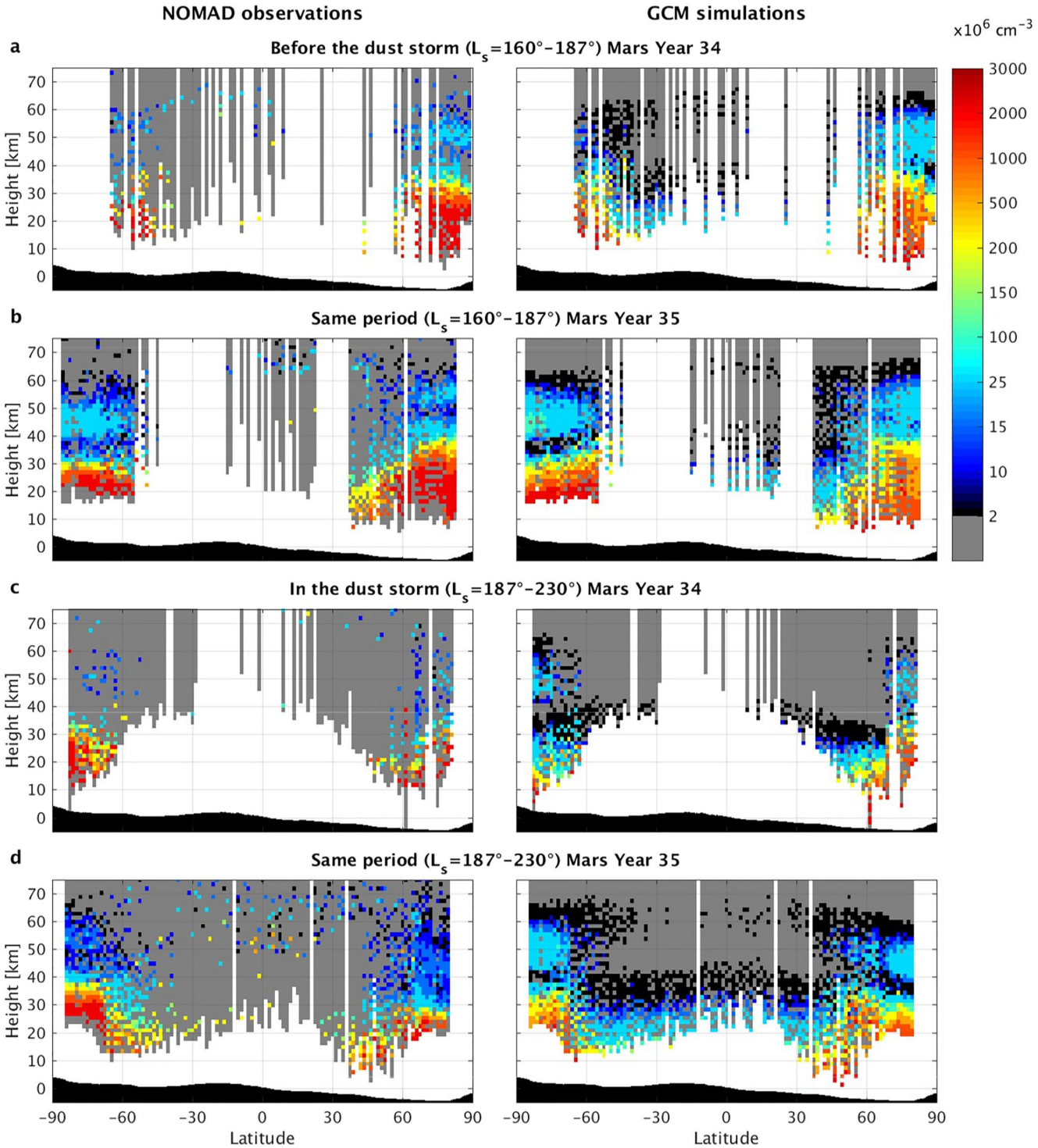

Figure 2. Latitude-height distribution of the ozone (O_3) number density profiles. Panels (a and b) show the average over L_s = 160°–187° and (c and d) over L_s = 187°–230°, in MY34 (a and c) and MY35 (b and d). The first period is before the global dust storm (GDS) in MY34, the second period covers the GDS in MY34. Left plots for the O_3 observed by NOMAD/UVIS and right ones from simulations. Gray shading: for the observations, this represents values that were filtered out (see Section 2); for the simulations, values are below 2×10^6 cm^{-3}. Height is with respect to the MOLA reference level (black shading shows zonally averaged MOLA topography). A grid of 1.5° in latitude and 1.5 km in height was used to compute the averages. Model results were interpolated to the time and location of the observations.

(Figure 2b) but with slightly reduced abundances. In MY34 however, ozone is strongly reduced immediately after the onset of the GDS for all heights above 20 km in the north and 30 km in the south (Figures 1a and 1c), consistent with the previous analyses (Khayat et al., 2021; Patel et al., 2021). This dramatic ozone reduction takes place at all latitudes, as can be seen in Figure 2c.

4. Atmospheric Chemistry Simulations

The differences in O_3 behavior between MY34 and MY35 have been qualitatively attributed to the observed increase of water vapor during the GDS at heights and latitudes that, in normal (non-GDS) conditions exhibit very low water vapor abundances (Patel et al., 2021). The enhanced high-altitude water vapor abundances lead to increased water vapor photolysis, producing odd hydrogen species that rapidly catalyze O_3 loss. However, the enhanced odd hydrogen species that are key to this process were not observable at the time. Without observational access to these radical species that drive the chemical pathways between water vapor and O_3, we turn to a model for atmospheric chemistry (Daerden et al., 2019; Neary & Daerden, 2018) to understand the enhanced destruction of O_3 during the GDS. Previous work has demonstrated how this model reproduced the redistribution of water vapor observed by NOMAD during the 2018 GDS (Neary et al., 2020). Here the model was run consecutively for MY34 and MY35. Both years were simulated using their respective daily dust optical depth climatologies (Montabone et al., 2015, 2020). For a direct comparison of model and data, the time-evolved 3D simulation results were interpolated in space and time to the NOMAD/UVIS observed O_3 profiles and added to Figures 1 and 2 in the same format as the data, but without filtering.

The resemblance of the model results to the O_3 observations is strong in morphology and often also in absolute values, providing evidence that the model captures well the underlying chemical processes. To understand these processes, Figure 3 shows the time-evolved simulation results of a range of key species (H_2O, OH, H, HO_2, O and O_3) at latitudes 60°N and 60°S in both Mars years. Figure 4 shows the global latitude-height cross-sections of the same species averaged over $L_s = 210°–220°$ (peak of the GDS in MY34) in both MY34 and MY35, and their relative change in this time window. (As the changes for odd hydrogen species between the 2 years are very large (ratio >1,000), we show them as a ratio. For O_3, the differences are smaller (ratio ∼< 20), and we show them as a percentage difference on a linear scale.) Both figures assist to the interpretation of Figures 1 and 2.

In the middle atmosphere, up to 100 km, and as low as 20 km at at low- and midlatitudes, down to 10 km north of of 45°N latitude, and down to the surface south 60°S, the O_3 abundances are severely reduced, up to 100% (Figure 4f, right panel, and Figure S8 in Supporting Information S1, right panels). This is a planet-wide O_3 destruction, taking place throughout almost the entire atmosphere, and demonstrates the massive impact of the GDS on the atmospheric composition.

Because water vapor is redistributed in a GDS from the lower atmosphere at low latitudes to the rest of the atmosphere (Neary et al., 2020), a small decrease in water vapor columns could be seen in measurements during previous GDS (M. D. Smith, 2004; M. Smith et al., 2018; Trokhimovskiy et al., 2015). As a consequence, we here simulate that O_3 abundances at low altitudes, low- and midlatitudes are increased (Figure 4f).

In terms of total O_3 columns, these changes are small in absolute terms, because (a) the air densities in the lowest atmosphere dominate the total column contribution, and (b) because total O_3 abundances in this season are small. But the changes are not small in relative terms. Figure S1 in Supporting Information S1 shows how the O_3 column at low latitudes is predicted to increase from below 1 to almost 2 μm-atm, this is a 100% increase. At high latitudes, the reduction of the O_3 column is up to 2 μm-atm, representing a 50% decrease in the north and a 100% decrease in the south.

Five reactions (see below) are dominating the change of the O_3 in the GDS. This change in O_3 follows the change in the relative strength of these reactions during the GDS (Figures S4 through S7 in Supporting Information S1 for reaction numbering and rates). Combined, they define the main pathway from enhanced water vapor to O_3 depletion, which can be described as follows:

1. The increase of water vapor in the middle and upper atmosphere and its subsequent photolysis ($H_2O + h\nu \rightarrow H + OH$, J11-13) results in the increased formation of atomic hydrogen (H) and OH radicals.
2. The OH radicals react with CO ($CO + OH \rightarrow CO_2 + H$, R1), and to a lesser extent with O ($O + OH \rightarrow O_2 + H$, R10), to cause an additional increase in atomic hydrogen.

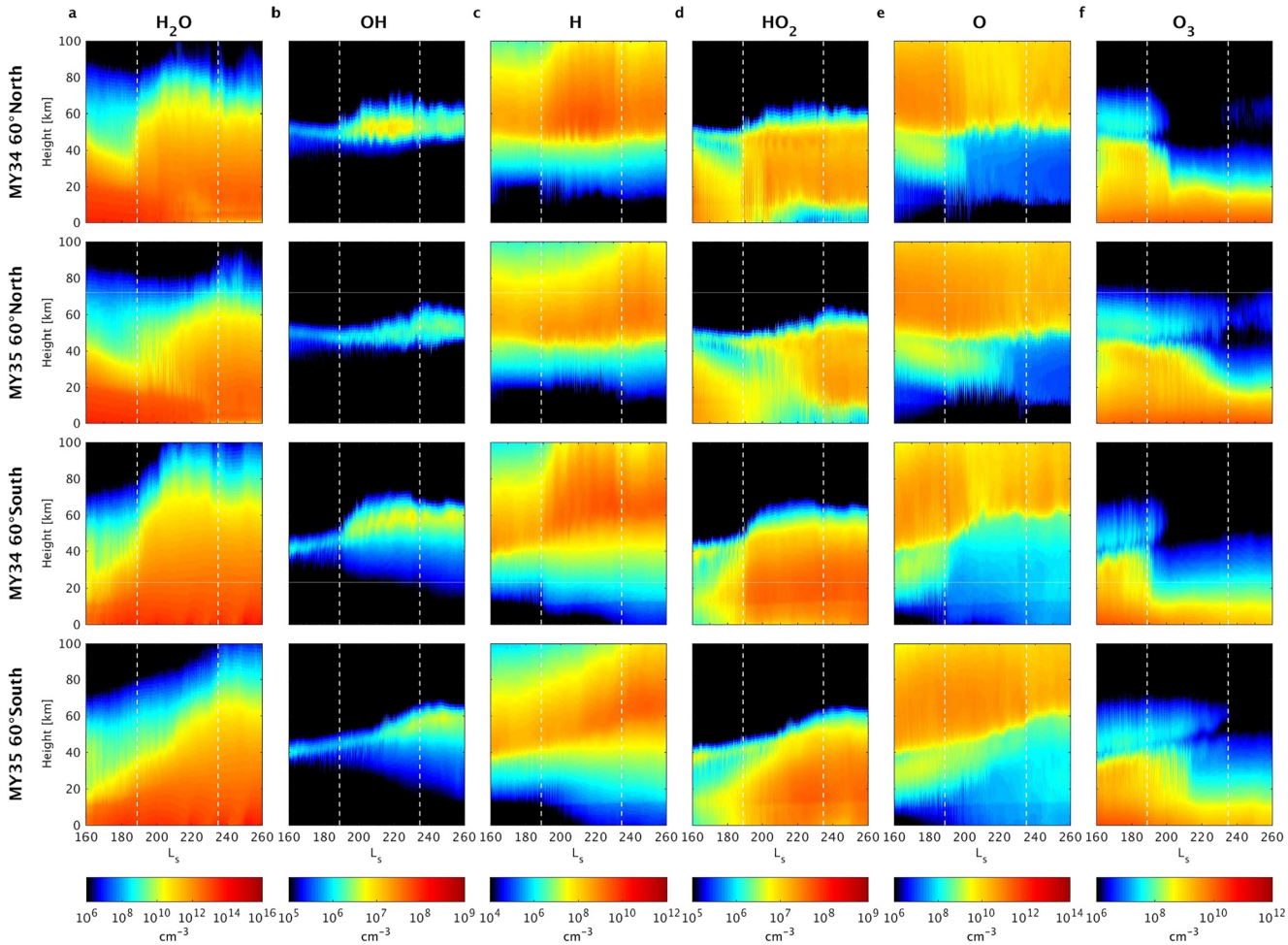

Figure 3. Simulated time series of H_2O, OH, H, HO_2, H and O_3 number densities for latitudes 60°N (top rows) and 60°S (bottom rows) around equinox, for Martian years 34 (with global dust storm, GDS) and 35 (no GDS). The color shading shows the number density averaged over all longitudes and local times. The dashed white lines indicate the onset and end of the GDS in MY34 and the same times in MY35.

3. Atomic hydrogen reacts with molecular oxygen ($H + O_2 + CO_2 \rightarrow HO_2 + CO_2$, R26) leading to an increase in HO_2.
4. HO_2 then reacts with atomic oxygen, O ($HO_2 + O \rightarrow OH + O_2$, R11) and so reduces the abundance of atomic oxygen. OH is returned to the atmosphere to resume step 2, and acts as a catalyzer.
5. Finally, the decrease in O suppresses the formation of O_3 in $O + O_2 + CO_2 \rightarrow O_3 + CO_2$ (R24)

The direct destruction of O_3 by HO_2 and OH is also enhanced in the GDS (Figure S7 in Supporting Information S1, R18 and R21), but only at high altitudes/latitudes, and not in the region of highest O_3 abundances, and so contributes less to the O_3 changes in the GDS.

The simulated time evolution of O_3 throughout the GDS as a result of these reactions, in comparison with the simulated evolution in MY35 and with the relative differences between both years, is shown Figure S8 in Supporting Information S1. An animation showing the model simulation of the O_3 vertical distribution in the GDS and one year later is also included in the Supporting Information S1.

A question to consider is to what extent the specific spatio-temporal distribution of the NOMAD observations (Figure S1 in Supporting Information S1) could have an impact on our results. In some cases, there are differences in coverage between MY34 and MY35, such as in the south before the GDS, or in the northern high-latitudes after $L_s \sim 200°$. However between $L_s \sim 215°$–$230°$, the coverage is similar in both years, so that the results shown in Figure 2 are robust. When considering only the profiles that are close in both L_s and latitude in both

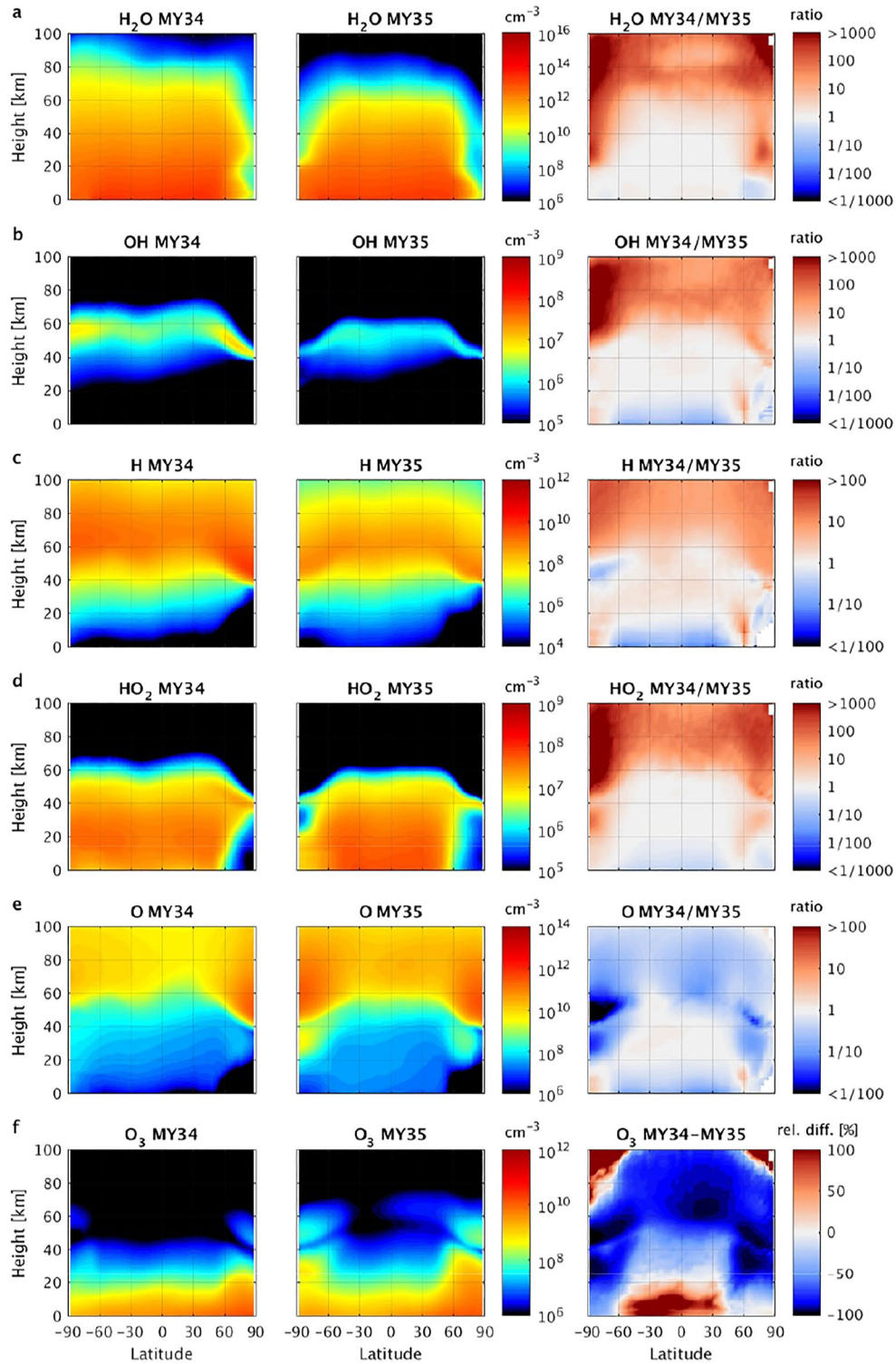

Figure 4. Latitude-height cross-sections of the simulated number densities of H_2O, OH, H, HO_2, O and O_3 for MY34 (left column) and MY35 (center column), averaged over L_s = 210°–220° (period which falls in the global dust storm (GDS) in MY34). The right column show the ratio of the averaged number densities in MY34 and MY35, except for O_3 for which the relative difference is shown. The densities from both years were first interpolated to a common altitude grid as the atmospheric height scale changed during the GDS.

years (Figures S9 and S10 in Supporting Information S1), there are more gaps in the figures, but they confirm our conclusions about how NOMAD witnessed O_3 loss in the 2018 GDS.

An interesting result from the simulations is the increased production of atomic hydrogen in the middle and upper atmosphere (Figures 3c and 4c), with increased number densities by factors of 10–100 above 60 km. This result (already preliminary shown in Neary et al., 2020) seems consistent with the observed enhanced abundance of atomic hydrogen in the upper atmosphere as observed by MAVEN during the 2018 global and regional dust storms (Chaffin et al., 2021; Stone et al., 2020).

5. Conclusions

The two endpoints of the above chain of reactions, water vapor and O_3, were observed by NOMAD before and during (MY34) and out of (MY35) the 2018 GDS (Aoki et al., 2019; Khayat et al., 2021; Patel et al., 2021). The model demonstrates the detailed chain of reactions occurring between these end points, involving unobserved odd hydrogen and oxygen species. The successful reproduction of the water vapor (Neary et al., 2020) and O_3 observations (this paper)—both end points in the chemistry chain—in very different conditions (in and out of a GDS), by the model provides support for the simulation of these unobserved species and the involved reactions. The simulated O_3 destruction in the GDS, supported by available observations, occurs throughout the middle atmosphere, that is, on a planet-wide scale. This shows the massive impact of the GDS and the redistribution of water vapor on atmospheric chemistry and composition, as the odd hydrogen radicals resulting from water vapor photolysis are highly reactive.

Interestingly, the simulated increase in the production of atomic hydrogen in the middle atmosphere during the GDS (Figures 3c and 4c) is important to understand the observed enhanced atmospheric escape during dust storms (Chaffin et al., 2021; Stone et al., 2020). It has been generally assumed that the redistribution of water vapor during GDS is causing the observed enhanced escape (Chaffin et al., 2021; Heavens et al., 2018; Shaposhnikov et al., 2021; Stone et al., 2020). While a dynamical perspective to understand the transport of water vapor to the upper atmosphere during a GDS was given in terms of wave activity (Yiğit, 2021), we provide here the photochemical processes that are also involved.

Data Availability Statement

ExoMars Trace Gas Orbiter data are publicly available through the European Space Agency's Planetary Science Archive (http://archives.esac.esa.int/psa) with additional access to NOMAD data through the PI institute (http://nomad.aeronomie.be). The NOMAD/UVIS Solar Occultation O_3 data set presented in this work, as well as the results from the General Circulation Model simulations are available on the BIRA-IASB data repository (https://repository.aeronomie.be/?doi=10.18758/71021070, Daerden & Wolff, 2022). The GEM-Mars General Circulation Model is based on the Global Environmental Multiscale model 4.2.0 version of the community weather forecasting model for Earth, which is one of the more recent versions available to the community, under the GNU Lesser General Public Licence v2.1. The adaptation for Mars is developed and maintained at the Royal Belgian Institute for Space Aeronomy.

Acknowledgments
This work was made possible thanks to the reconstructed gridded maps of column dust optical depth from Mars Climate Sounder observations provided by L. Montabone. The dust maps were prepared using MCS v5.3 provided by A. Kleinböhl and D. Kass. Dust climatologies can be found at the following link: http://www-mars.lmd.jussieu.fr/mars/dust_climatology/. ExoMars is a space mission of the European Space Agency (ESA) and Roscosmos. The NOMAD experiment is led by the Royal Belgian Institute for Space Aeronomy (IASB-BIRA), assisted by Co-PI teams from Spain (IAA-CSIC), Italy (INAF-IAPS), and the United Kingdom (Open University). This project acknowledges funding by the Belgian Science Policy Office (BELSPO), with the financial and contractual coordination by the ESA Prodex Office (PEA 4000103401, 4000121493), by the UK Space Agency (grants ST/V002295/1, ST/P001262/1, ST/V005332/1 and ST/S00145X/1), by the Spanish Ministry of Science and Innovation (MCIU), and by European funds (grants PGC2018-101836-B-I00 and ESP2017-87143-R, MINECO/FEDER), as well as by the Italian Space Agency (Grant 2018-2-HH.0). This work was supported by the Belgian Fonds de la Recherche Scientifique – FNRS (Grant Nos. 30442502, ET_HOME). This work has received funding from the European Union's Horizon 2020 research and innovation programme (grant agreement No 101004052, RoadMap project). The IAA/CSIC team acknowledges financial support from the State Agency for Research of the Spanish MCIU through the "Center of Excellence Severo Ochoa" award for the Instituto de Astrofísica de Andalucía (SEV-2017-0709). US investigators were supported by the National Aeronautics and Space Administration, by NASA's Mars Program Office (under WBS 604796, "Participation in the TGO/NOMAD Investigation of Trace Gases on Mars."), and by NASA (award number 80GSFC21M0002). Canadian investigators were supported by the Canadian Space Agency. We thank Manuel López Puertas and two anonymous reviewers for useful comments on the manuscript.

References

Aoki, S., Vandaele, A. C., Daerden, F., Villanueva, G. L., Liuzzi, G., Thomas, I. R., et al. (2019). Water vapor vertical profiles on Mars in dust storms observed by TGO/NOMAD. *Journal of Geophysical Research: Planets*, *124*(12), 3482–3497. https://doi.org/10.1029/2019JE006109

Chaffin, M. S., Kass, D. M., Aoki, S., Fedorova, A. A., Deighan, J., Connour, K., et al. (2021). Martian water loss to space enhanced by regional dust storms. *Nature Astronomy*, *5*(10), 1036–1042. https://doi.org/10.1038/s41550-021-01425-w

Clancy, R. T., & Nair, H. (1996). Annual (perihelion–aphelion) cycles in the photochemical behavior of the global Mars atmosphere. *Journal of Geophysical Research*, *101*(E5), 12785–12790. https://doi.org/10.1029/96je00836

Clancy, R. T., Wolff, M. J., Lefevre, F., Cantor, B. A., Malin, M. C., & Smith, M. D. (2016). Daily global mapping of Mars ozone column abundances with MARCI UV band imaging. *Icarus*, *266*, 112–133. https://doi.org/10.1016/j.icarus.2015.11.016

Daerden, F., Neary, L., Villanueva, G., Liuzzi, G., Aoki, S., Clancy, R. T., et al. (2022). Explaining NOMAD D/H observations by cloud-induced fractionation of water vapor on Mars. *Journal of Geophysical Research: Planets*, *127*(2), e2021JE007079. https://doi.org/10.1029/2021JE007079

Daerden, F., Neary, L., Viscardy, S., García Muñoz, A., Clancy, R. T., Smith, M. D., et al. (2019). Mars atmospheric chemistry simulations with the GEM-Mars general circulation model. *Icarus*, *326*, 197–224. https://doi.org/10.1016/j.icarus.2019.02.030

Daerden, F., & Wolff, M. J. (2022). NOMAD/UVIS ozone retrievals and GEM-Mars GCM simulations of ozone on Mars during the 2018 global dust storm and one year later, for Daerden et al., [Data set]. Royal Belgian Institute for Space Aeronomy (BIRA-IASB). https://doi.org/10.18758/71021070

Fedorova, A., Bertaux, J.-L., Betsis, D., Montmessin, F., Korablev, O., Maltagliati, L., & Clarke, J. (2018). Water vapor in the middle atmosphere of Mars during the 2007 global dust storm. *Icarus*, *300*, 440–457. https://doi.org/10.1016/j.icarus.2017.09.025

Fedorova, A., Montmessin, F., Korablev, O., Lefevre, F., Trokhimovskiy, A., & Bertaux, J. L. (2021). Multi-annual monitoring of the water vapor vertical distribution on Mars by SPICAM on Mars Express. *Journal of Geophysical Research: Planets*, *126*(1), e2020JE006616. https://doi.org/10.1029/2020JE006616

Fedorova, A. A., Montmessin, F., Korablev, O., Luginin, M., Trokhimovskiy, A., Belyaev, D. A., et al. (2020). Stormy water on Mars: The distribution and saturation of atmospheric water during the dusty season. *Science*, *367*(6475), 297–300. https://doi.org/10.1126/science.aay9522

Gérard, J.-C., Aoki, S., Willame, Y., Gkouvelis, L., Depiesse, C., Thomas, I. R., et al. (2020). Detection of green line emission in the dayside atmosphere of Mars from NOMAD-TGO observations. *Nature Astronomy*, *4*(11), 1049–1052. https://doi.org/10.1038/s41550-020-1123-2

Heavens, N. G., Kleinböhl, A., Chaffin, M. S., Halekas, J. S., Kass, D. M., Hayne, P. O., et al. (2018). Hydrogen escape from Mars enhanced by deep convection in dust storms. *Nature Astronomy*, *2*, 126–132. https://doi.org/10.1038/s41550-017-0353-4

Khayat, A. S. J., Smith, M. D., Wolff, M., Daerden, F., Neary, L., Patel, M. R., et al. (2021). ExoMars TGO/NOMAD-UVIS vertical profiles of ozone: 2. The high-altitude layers of atmospheric ozone. *Journal of Geophysical Research: Planets*, *126*(11), e2021JE006834. https://doi.org/10.1029/2021JE006834

Korablev, O., Vandaele, A. C., Montmessin, F., Fedorova, A. A., Trokhimovskiy, A., Forget, F., et al. (2019). No detection of methane on Mars from early ExoMars Trace Gas Orbiter observations. *Nature*, *568*(7753), 517–520. https://doi.org/10.1038/s41586-019-1096-4

Korablev, O. I., Montmessin, F., Trokhimovskiy, A., Fedorova, A. A., Shakun, A. V., Grigoriev, A. V., et al. (2018). The atmospheric chemistry suite (ACS) of three spectrometers for the ExoMars 2016 trace gas orbiter. *Space Science Reviews*, *214*(1), 7. https://doi.org/10.1007/s11214-017-0437-6

Lebonnois, S., Quemerais, E., Montmessin, F., Lefevre, F., Perrier, S., Bertaux, J. L., & Forget, F. (2006). Vertical distribution of ozone on Mars as measured by SPICAM/Mars Express using stellar occultations. *Journal of Geophysical Research*, *111*(E9), E09S05. https://doi.org/10.1029/2005JE002643

Lefèvre, F., Lebonnois, S., Montmessin, F., & Forget, F. (2004). Three-dimensional modeling of ozone on Mars. *Journal of Geophysical Research*, *109*(E7), E07004. https://doi.org/10.1029/2004JE002268

Lefèvre, F., Trokhimovskiy, A., Fedorova, A., Baggio, L., Lacombe, G., Maattanen, A., et al. (2021). Relationship between the ozone and water vapour columns on Mars as observed by SPICAM and calculated by a global climate model. *Journal of Geophysical Research: Planets*, *126*(4), e2021JE006838. https://doi.org/10.1029/2021JE006838

Markwardt, C. (2009). Non-linear least squares fitting in IDL with MPFIT. In *Astronomical Data Analysis Software and Systems XVIII ASP Conference Series*, In D. A. Bohlender, D. Durand, & P. Dowler (Eds.) (Vol. 411) 251. Astronomical Society of the Pacific. Retrieved from https://arxiv.org/abs/0902.2850

McElroy, M. B., & Donahue, T. M. (1972). Stability of the Martian atmosphere. *Science*, *177*(4053), 986–988. https://doi.org/10.1126/science.177.4053.986

Montabone, L., Forget, F., Millour, E., Wilson, R. J., Lewis, S. R., Cantor, B., et al. (2015). Eight-year climatology of dust optical depth on Mars. *Icarus*, *251*, 65–95. https://doi.org/10.1016/j.icarus.2014.12.034

Montabone, L., Spiga, A., Kass, D. M., Kleinböhl, A., Forget, F., & Millour, E. (2020). Martian year 34 column dust climatology from Mars climate sounder observations: Reconstructed maps and model simulations. *Journal of Geophysical Research: Planets*, *125*(8). https://doi.org/10.1029/2019JE006111

Montmessin, F., Korablev, O., Lefevre, F., Bertaux, J. L., Fedorova, A., Trokhimovskiy, A., et al. (2017). SPICAM on Mars express: A 10 year in-depth survey of the Martian atmosphere. *Icarus*, *297*, 195–216. https://doi.org/10.1016/j.icarus.2017.06.022

Montmessin, F., & Lefèvre, F. (2013). Transport-driven formation of a polar ozone layer on Mars. *Nature Geoscience*, *6*(11), 930–933. https://doi.org/10.1038/ngeo1957

Neary, L., & Daerden, F. (2018). The GEM-Mars general circulation model for Mars: Description and evaluation. *Icarus*, *300*, 458–476. https://doi.org/10.1016/j.icarus.2017.09.028

Neary, L., Daerden, F., Aoki, S., Whiteway, J., Clancy, R. T., Smith, M., et al. (2020). Explanation for the increase in high-altitude water on Mars observed by NOMAD during the 2018 global dust storm. *Geophysical Research Letters*, *47*(7), e2019GL084354. https://doi.org/10.1029/2019GL084354

Olsen, K. S., Lefèvre, F., Montmessin, F., Trokhimovskiy, A., Baggio, L., Fedorova, A., et al. (2020). First detection of ozone in the mid-infrared at Mars: Implications for methane detection. *Astronomy & Astrophysics*, *639*, A141. https://doi.org/10.1051/0004-6361/202038125

Parkinson, T. D., & Hunten, D. M. (1972). Spectroscopy and aeronomy of O_2 on Mars. *Journal of the Atmospheric Sciences*, *29*(7), 1380–1390. https://doi.org/10.1175/1520-0469(1972)029<1380:saaooo>2.0.co;2

Patel, M. R., Antoine, P., Mason, J., Leese, M., Hathi, B., Stevens, A. H., et al. (2017). NOMAD spectrometer on the ExoMars trace gas orbiter mission: Part 2—Design, manufacturing, and testing of the ultraviolet and visible channel. *Applied Optics*, *56*(10), 2771–2782. https://doi.org/10.1364/AO.56.002771

Patel, M. R., Sellers, G., Mason, J. P., Holmes, J. A., Brown, M. A. J., Lewis, S. R., et al. (2021). ExoMars TGO/NOMAD-UVIS vertical profiles of ozone: 1. Seasonal variation and comparison to water. *Journal of Geophysical Research: Planets*, *126*(11), e2021JE006837. https://doi.org/10.1029/2021JE006837

Perrier, S., Bertaux, J. L., Lefevre, F., Lebonnois, S., Korablev, O., Fedorova, A., & Montmessin, F. (2006). Global distribution of total ozone on Mars from SPICAM/MEX UV measurements. *Journal of Geophysical Research*, *111*(E9), E09S06. https://doi.org/10.1029/2006JE002681

Rodgers, C. D. (2000). *Inverse methods for atmospheric sounding*. World Science.238

Sander, S. P., Abbatt, J., Barker, J. R., Burkholder, J. B., Friedl, R. R., Golden, D. M., et al. (2011). *Chemical kinetics and photochemical data for use in atmospheric studies*. Technical Report Evaluation No 17, Publication 10-6. Jet Propulsion Laboratory. Retrieved from http://jpldataeval.jpl.nasa.gov

Shaposhnikov, D. S., Medvedev, A. S., & Rodin, A. V. (2021). Simulation of water vapor photodissociation during dust storm season on Mars. *Solar System Research*, *56*(1), 23–31. https://doi.org/10.1134/s0038094622010051

Smith, D. E., Zuber, M. T., Solomon, S. C., Phillips, R. J., Head, J. W., Garvin, J. B., et al. (1999). The global topography of Mars and implications for surface evolution. *Science*, *284*(5419), 1495–1503. https://doi.org/10.1126/science.284.5419.1495

Smith, M. D. (2004). Interannual variability in TES atmospheric observations of Mars during 1999–2003. *Icarus*, *167*(1), 148–165. https://doi.org/10.1016/j.icarus.2003.09.010

Smith, M. D. (2019). THEMIS observations of the 2018 Mars global dust storm. *Journal of Geophysical Research: Planets*, *124*(11), 2929–2944. https://doi.org/10.1029/2019JE006107

Smith, M., Daerden, F., Neary, L., & Khayat, S. (2018). The climatology of carbon monoxide and water vapour on Mars as observed by CRISM and modeled by the GEM-Mars general circulation model. *Icarus*, *301*, 117–131. https://doi.org/10.1016/j.icarus.2017.09.027

Stcherbinine, A., Vincendon, M., Montmessin, F., Wolff, M. J., Korablev, O., Fedorova, A., et al. (2020). Martian water ice clouds during the 2018 global dust storm as observed by the ACS-MIR channel onboard the Trace Gas Orbiter. *Journal of Geophysical Research: Planets*, *125*(3), e2019JE006300. https://doi.org/10.1029/2019JE006300

Stone, S. W., Yelle, R. V., Benna, M., Lo, D. Y., Elrod, M. K., & Mahaffy, P. R. (2020). Hydrogen escape from Mars is driven by seasonal and dust storm transport of water. *Science*, *370*(6518), 824–831. https://doi.org/10.1126/science.aba5229

Trokhimovskiy, A., Fedorova, A., Korablev, O., Montmessin, F., Bertaux, J. L., Rodin, A., & Smith, M. D. (2015). Mars' water vapour mapping by the SPICAM IR spectrometer: Five Martian years of observations. *Icarus*, *251*, 50–64. https://doi.org/10.1016/j.icarus.2014.10.007

Vandaele, A. C., Korablev, O., Daerden, F., Aoki, S., Thomas, I. R., Altieri, F., et al. (2019). Martian dust storm impact on atmospheric H_2O and D/H observed by ExoMars Trace Gas Orbiter. *Nature*, *568*(7753), 521–525. https://doi.org/10.1038/s41586-019-1097-3

Vandaele, A. C., Lopez-Moreno, J. J., Patel, M. R., Bellucci, G., Daerden, F., Ristic, B., et al. (2018). NOMAD, an integrated suite of three spectrometers for the ExoMars trace gas mission: Technical description, science objectives and expected performance. *Space Science Reviews*, *214*(5), 80. https://doi.org/10.1007/s11214-018-0517-2

Willame, Y., Vandaele, A., Depiesse, C., Lefevre, F., Letocart, V., Gillotay, D., & Montmessin, F. (2017). Retrieving cloud, dust and ozone abundances in the Martian atmosphere using SPICAM/UV nadir spectra. *Planetary and Space Science*, *142*, 9–25. https://doi.org/10.1016/j.pss.2017.04.011

Yiğit, E. (2021). Martian water escape and internal waves. *Science*, *374*(6573), 1323–1324. https://doi.org/10.1126/science.abg5893